analytical chemistry

pubs.acs.org/ac Article

Nucleic Acid Quantification with Amplicon Yield in Recombinase Polymerase Amplification

Priyanka Valloly and Rahul Roy*

Cite This: *Anal. Chem.* 2022, 94, 13897−13905 Read Online

ACCESS | Metrics & More | Article Recommendations | Supporting Information

ABSTRACT: Amplification-based quantitative polymerase chain reaction (qPCR) provides accurate and sensitive nucleic acid quantification. However, the requirement of temperature cycling and real-time monitoring limits its translation to many settings. Quantitative isothermal amplification methods alleviate the need for thermal cyclers; however, they still require continuous monitoring of the nucleic acid amplification on sophisticated readers. Here, we adapted an isothermal recombinase polymerase amplification (RPA) reaction to develop a semiquantitative method that relies on the final amplicon yield to estimate the initial target nucleic acid copy number. To achieve this, we developed a phenomenological model that captures the essential RPA dynamics. We identified reaction conditions that constrained the reaction yield corresponding to the starting DNA template concentration. We validated these predictions experimentally and showed that the amplicon yields at the end of the RPA reaction correlated well with the starting DNA concentration while reducing nonspecific amplification robustly. We demonstrate this approach, termed quantitative endpoint RPA (qeRPA), to detect DNA over five log orders with a detection limit of 100 molecules. Using a linear regression model of the normalized endpoint intensity (NEI) standard curve, we estimate the viral load from the serum of dengue virus-infected patients with comparable performance to qPCR. Unlike the conventional isothermal quantitative methods, qeRPA can be employed for robust and sensitive nucleic acid estimation at close to room temperature without real-time monitoring and can be beneficial for field deployment in resource-limited settings.

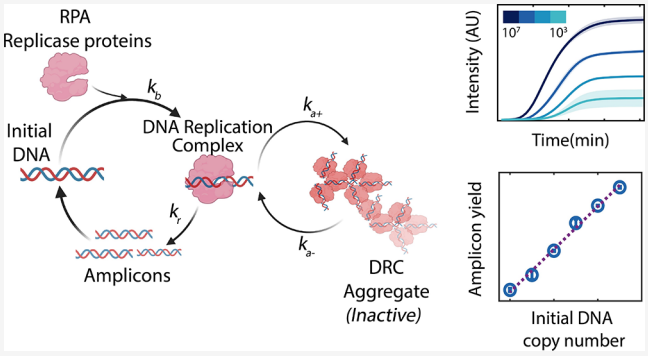

Downloaded via INDIAN INST OF SCIENCE on October 31, 2022 at 05:47:21 (UTC).
See https://pubs.acs.org/sharingguidelines for options on how to legitimately share published articles.

■ INTRODUCTION

Nucleic acid quantification is crucial for gene expression analysis, detection of rare or dysfunctional cells, monitoring pathogen load during infections, and assessing treatment outcomes.[1−3] Quantitative polymerase chain reaction (qPCR) has long been the gold standard for quantitative nucleic acid analysis.[4,5] Since the key observable threshold cycle (C_t) estimate is dependent on the efficiency and kinetics of the polymerization reaction, qPCR requires careful calibration and continuous monitoring of the amplification reaction. More importantly, the necessity for thermal cycling makes its implementation difficult in resource-limited settings. The recent advent of several isothermal nucleic acid amplification techniques (INAATs) alleviates the need for thermal cycling and hence offers promising alternatives to qPCR.[6] INAATs like loop-mediated isothermal amplification (LAMP),[7] helicase-dependent amplification (HDA),[8] and strand displacement amplification (SDA)[9] can generate detectable amplicons in less than an hour. Using the time to reach amplicon levels beyond the threshold of detection, τ_d, INAATs can also report the estimates of the initial DNA concentration.[10] For example, the LAMP assay has reported quantifiable DNA in the range of $10-10^7$ copies/μL.[11] However, the current INAAT approaches rely on the time to the onset of amplification for quantification, thus requiring real-time monitoring. Further, rapid amplification requires tight temporal control in such assays, and rapid generation of spurious nonspecific products mandates the use of specific probes. These limitations pose major challenges for the design and development of a robust and field-deployable DNA quantification with INAATs.

Another promising INAAT, recombinase polymerase amplification (RPA), works close to ambient temperature (37−42 °C) and requires two end-specific primers with a cocktail of recombinase, single-strand binding protein, and a strand displacement DNA polymerase.[12,13] Recombinase bound to the primers assists in homology search and strand exchange. This allows the primers to rapidly anneal to their cognate target site and recruit the other proteins. The DNA polymerase then extends the primer in a 5′−3′ direction while displacing the nontemplate strand. Multiple DNA proteins and

Received: June 29, 2022
Accepted: September 15, 2022
Published: September 28, 2022

ACS Publications © 2022 American Chemical Society

https://doi.org/10.1021/acs.analchem.2c02810
Anal. Chem. 2022, 94, 13897−13905

high concentration of primers under the action of crowding agents lead to the rapid formation of the product with high sensitivity. Indeed, it has been shown that a single molecule of target DNA can be detected with RPA within 30 min.[14] Yet, most successfully developed RPA assays are qualitative with a positive/negative readout for target DNA, and τ_d-based quantification from real-time RPA kinetic measurements has found limited success.[14−16] This partly arises due to the poor control over undesired amplification close to the ambient temperature after initiation.[17] Similarly, a common observation with RPA reactions has been the low and variable yield of amplicons compared to PCR, though the underlying factors contributing to this remain uncharacterized. To bypass these issues and reduce interference from nonspecific amplicons, a recent report presented a competitive RPA scheme where a reference DNA competes with the target for primers and amplification enzymes.[18] Amplicon levels compared to the reference were employed to demonstrate quantification over five log orders. However, such ratiometric techniques require optimized reference templates and additional probes to quantify the reference DNA and hence are challenging to implement.

Development of INAATs can benefit from mathematical kinetic models based on a mechanistic understanding of the reaction pathway that can identify the parameters controlling the amplification kinetics and yield of amplicons.[19−21] However, most existing mathematical treatments of RPA propose ways to improve the τ_d-based detection or the kinetic parameter estimation from real-time amplification trajectories.[15,22] Recently, a mechanism-based kinetic model for RPA described how mixing is a key limitation controlling the amplification reaction, but the model focused on the initial reaction conditions to improve τ_d-based quantification.[20]

In this work, we overcome the reliance on real-time monitoring for quantification and develop a semiquantitative endpoint (qe)RPA that can estimate the target DNA amount over five log orders with the final amplicon measurement. We developed a kinetic model for RPA using insights from fluorescence imaging and real-time monitoring of RPA reactions. We show that rapid DNA polymerization progressively leads to the formation of DNA amplicon clusters that limit further amplification. A key prediction from our model suggests that the yield of the RPA amplicons would be dependent on the initial target DNA concentration as the kinetics of amplification becomes comparable to the DNA cluster formation. We experimentally validate this and report that apart from the threshold time, the amplicon yield can display a linear relationship with the log of the starting DNA concentration. We optimized the RPA reaction to identify the conditions that increase the sensitivity and resolution of our assay as well as demonstrate the robustness of the method. Our semiquantitative endpoint (qeRPA) can estimate the target DNA with a detection limit of 100 molecules. Importantly, qeRPA mitigates the need for real-time monitoring, lowers background amplification, and enables the use of a DNA-intercalating dye for quantification. Finally, we demonstrate that qeRPA can determine the viral load from the clinical serum samples from dengue patients over a wide concentration range consistent with the matched qPCR estimates. Overall, we present an easy-to-deploy variant of quantitative INAAT that is suited for nucleic acid measurement in the field.

■ MATERIALS AND METHODS

Nucleic Acids for Amplification. We use the plasmid pRL02 as a template for both the qeRPA assay and standard curve generation when not mentioned otherwise. It codes for partial segments of the dengue virus serotype 2 (DENV2) genome (NCBI GenBank: AY037116.1, genome nucleotide positions from 1 to 403, 10,120 to 10,723) inserted in a pUC57 backbone. The pRL02 plasmid was isolated (Qiagen plasmid isolation kit) from DH5α *E. coli* and eluted in nuclease-free water.

For viral load quantification, DENV2 viral RNA was isolated from 250 μL of leftover serum (collected from patients who tested positive with the dengue NS1 antigen test, J.Mitra Co.) in the Dengue Consortium Study in Bangalore, India. Informed consent from patients was received as per study protocols approved by the Institute Ethics Committees where samples were collected, and assays were performed. Extracted RNA (Qiagen viral RNA purification kit) was eluted in nuclease-free water as per manufacturer's instructions. All samples were serotyped as DENV2 using a real-time RT-PCR kit (Geno-Sen's DENGUE 1−4 Real-Time PCR Kit). The viral RNA from the patient samples was reverse transcribed with the primer DENV-CRP with the SuperScript IV reverse transcriptase according to manufacturer's instructions (Invitrogen). All template nucleic acids were quantified using Qubit-4.

Primers. Primers (FW-535, RW-837) targeting the DENV2 capsid gene (GenBank: 3AY037116.1, nucleotide positions from 98 to 403) were designed and used for RPA standardization assays. For viral load quantification from clinical samples, separate RPA primers (DENV-CFP4, DENV-CRP) were designed for the conserved regions of the capsid gene based on 15 India-specific DENV2 genome sequences (NCBI GenBank). Alignment of the sequences was done in UGENE software, and the primers were designed using the IDT OligoAnalyzer tool. The detection probe was designed according to the manufacturer's recommendation targeting the capsid region of DENV2 with TAMRA dye and BHQ-2 quencher. Designed primers conform to the following criteria: (i) 30−35 bases in length, (ii) 30−70% GC content, and (iii) minimum Gibbs free energy (ΔG) allowed for hairpin structures, homodimer and heterodimer formation is −4 kJmol^{-1}. All the primer and probe sequences are listed in Table S1.

qPCR Assay. cDNA from reverse transcription of DENV2 clinical viral RNA was quantified using qPCR with the KAPA2G Robust HotStart ReadyMix, 500 nM primers (DENV-CFP4 and DENV-CRP), 2.04 μM EvaGreen dye (Biotium), and cDNA template (pRL02). The qPCR reaction (Bio-Rad, CFX96 Touch) was performed as follows: 95 °C for 3 min, followed by 35 cycles at 95 °C for 15 s, 66 °C for 15 s, and 72 °C for 20 s with a final extension at 72 °C for 30 s. The real-time trajectories obtained from the qPCR thermocycler (Bio-Rad, CFX96 Touch) were analyzed using a custom-written MATLAB script by building a standard curve with template (pRL02) copy number and threshold cycle.

RPA Reaction. All RPA reactions were carried out using the TwistAmp Basic kit (TwistDX). For the unmodified RPA reaction, one RPA enzyme pellet was resuspended in 29.5 μL of rehydration buffer and supplemented with 300 nM primers (FP-535 and RP-837) and 2.04 μM EvaGreen dye. The mixture was then vortexed and centrifuged, followed by the

https://doi.org/10.1021/acs.analchem.2c02810
Anal. Chem. 2022, 94, 13897−13905

addition of template, 14 mM magnesium acetate, and nuclease-free water to a total volume of 50 μL. The reaction was kept on ice until the start of RPA. The RPA mix was incubated at 39 °C when not mentioned otherwise and was monitored in real time (Bio-Rad, CFX96 Touch). The optimized qeRPA reaction consists of one RPA pellet resuspended to a final volume of 100 μL with 300 nM primers, supplemented with additional reagents to prepare the qeRPA cocktail comprising of 2.4 mM ATP, 0.24 mM dNTP, 2.04 μM EvaGreen dye, 14 mM magnesium acetate, template nucleic acid, and TD buffer (25 mM Tris (pH 7.9) and 3 mM DTT). These modified qeRPA reaction conditions were used when not mentioned otherwise. To compare the effect of detection strategy, EvaGreen DNA dye was replaced with RPA fluorescent probes (DENV2-CAP-probe at 0.12 μM) with 100 U exonuclease III (NEB), keeping all other reagents the same. To test the RPA specificity, the pRL02 plasmid in the presence of varying concentrations of mammalian genomic DNA (extracted from Vero E6 cells, ATCC CRL-1586) was used as the template.

Model for RPA Dynamics. The major steps in the RPA reaction considered in our model are depicted in Figure 2A. The model simplifies the RPA reaction with insights from experiments, and molecular steps are lumped to capture only the key features of the amplification process. Some of the key model assumptions are discussed in the following: (i) The reactants such as ATP, dNTP, primer, and enzyme are not limiting in concentration. This assumption is likely not valid at the later stages of the amplification (as discussed later). However, it is reasonable since we observe an insignificant increase in amplicons upon their addition after the formation of clusters. (ii) DNA proteins bind to the primers quickly. This is justified by usually high association rates observed for recombinases and DNA polymerases[23−25] and high concentration of enzymes and primers in the reaction mix.

The RPA reaction is represented by three distinct steps. First, the pre-amplification step includes the recombinase-primer complex binding to the target dsDNA (D), and further binding of the polymerase to the above complex generates the DNA-replication complex (DRC) (Figure 2A). Second, DRC, upon polymerization, generates new amplicon DNA. Third, the DRC can reversibly generate larger polymerization-incompetent aggregates called DRC aggregate ($\mathrm{DRC_A}$) due to the condensation of DNA and proteins during the reaction.

The rate equations used to simulate the kinetics of the reaction are given as follows:

$$\frac{d\mathrm{DRC}}{dt} = k_b DP - (k_{a+}\mathrm{DRC}^2 - k_{a-}\mathrm{DRC_A}) \tag{1}$$

$$\frac{dP}{dt} = -k_b DP \tag{2}$$

$$\frac{dD}{dt} = -k_b DP + k_r \mathrm{DRC}\left(1 - \frac{\mathrm{DRC_A}}{\mathrm{DRC_{At}}}\right)\left(\frac{P}{P_m} - 1\right) \tag{3}$$

$$\frac{d\mathrm{DRC_A}}{dt} = k_{a+}\mathrm{DRC}^2 - k_{a-}\mathrm{DRC_A} \tag{4}$$

where D, DRC and $\mathrm{DRC_A}$ denote the number of free dsDNA, the DNA−protein complex for polymerization, and the inactive form of DNA-enzyme aggregate and P represents the DNA proteins in the reaction mixture. k_b and k_r are the rate constants for the DRC formation and polymerization of new DNA, respectively. k_{a+} and k_{a-} are the rates for formation and recovery from the inactive $\mathrm{DRC_A}$ state. We assume k_b to be high (0.1−100 molecule^{-1} s^{-1}) consistent with tight binding observed for most DNA-binding proteins in RPA. In comparison, k_{a+} is set as 0.001 molecule^{-1} s^{-1} and k_{a-} was varied between 0.0075 and 0.0001 s^{-1} to instantiate different aggregation scenarios. We also impose two constraints to match the reaction conditions. DNA amplification reaches saturation either when it hits the threshold level of $\mathrm{DRC_A}$ ($\mathrm{DRC_{At}}$) or when most of the free proteins are bound to DNA (implemented as the minimal protein level required for successful polymerization (P_m)). Both control the effective polymerization rate in a logistic fashion (second term in eq 3). We assume the levels of $\mathrm{DRC_{At}}$ to be high and use rough estimates (20,000 molecules) as limited experimental data is available at present. Similarly, the reaction stalls as the protein levels drop and approach P_m (set as 10,000 molecules). D_{all} (= D + DRC + $\mathrm{DRC_A}$) represents the total DNA in the reaction mixture, and it is plotted in the results for comparison of the amplification kinetics. Changes in $\mathrm{DRC_{At}}$ and P_m influence the final range of amplicon yields and time to saturation; however, the overall amplicon dependence on the initial level of target DNA is reproduced.

Analysis of RPA Amplification Trajectories. The real-time amplification kinetics for RPA reactions was extracted and analyzed using the custom-written MATLAB script. Briefly, the raw fluorescence time trajectories were fit to a four-parameter logistic equation (eq 5) after background subtraction (background is set as the intensity value at t = 0):

$$F(t) = F_0 + \frac{F_{\max} - F_0}{1 + \left(\frac{t}{t_{1/2}}\right)^d} \tag{5}$$

where $F(t)$ represents the fluorescence intensity as a function of time (t). $F_{\max}$ and F_0 represent the saturation and baseline intensity, respectively. The variables $t_{1/2}$ and d denote the point of inflection (time point corresponding to half of the intensity difference between $F_{\max}$ and F_0) and the steepness (or slope) of the curve at $t_{1/2}$, respectively (Figure 3B). From these parameters, the threshold time point (TP) is derived as the convergence point of P1 (tangent to F_0) and P2 (tangent at $t_{1/2}$) corresponding to the linear part of amplification, as given by eq 6, which is analytically derived by solving the line equations for P1 and P2 (Supplementary note S2):[26]

$$TP = t_{1/2} + \frac{(2 + d)}{d} \tag{6}$$

Finally, we define the normalized endpoint intensity (NEI) and normalized threshold time (NTT) as shown below:

$$\mathrm{NEI} = \frac{F_{\max}(n)}{F_{\max}(\mathrm{NTC})} \tag{7}$$

$$\mathrm{NTT} = \frac{TP\ (\mathrm{NTC})}{TP\ (n)} \tag{8}$$

where n and NTC denote the target DNA levels and negative control with no template DNA.

Imaging and Data Analysis. The RPA-amplified mixture was imaged on an inverted epifluorescence microscope to capture the fluorescence intensity from EvaGreen dye-bound dsDNA. The imaging glass coverslip surface was treated with dichlorodimethylsilane[27] (DDS) (Sigma-Aldrich: 440272) and further passivated with 2 mg/mL bovine serum albumin (BSA;

https://doi.org/10.1021/acs.analchem.2c02810
Anal. Chem. 2022, 94, 13897−13905

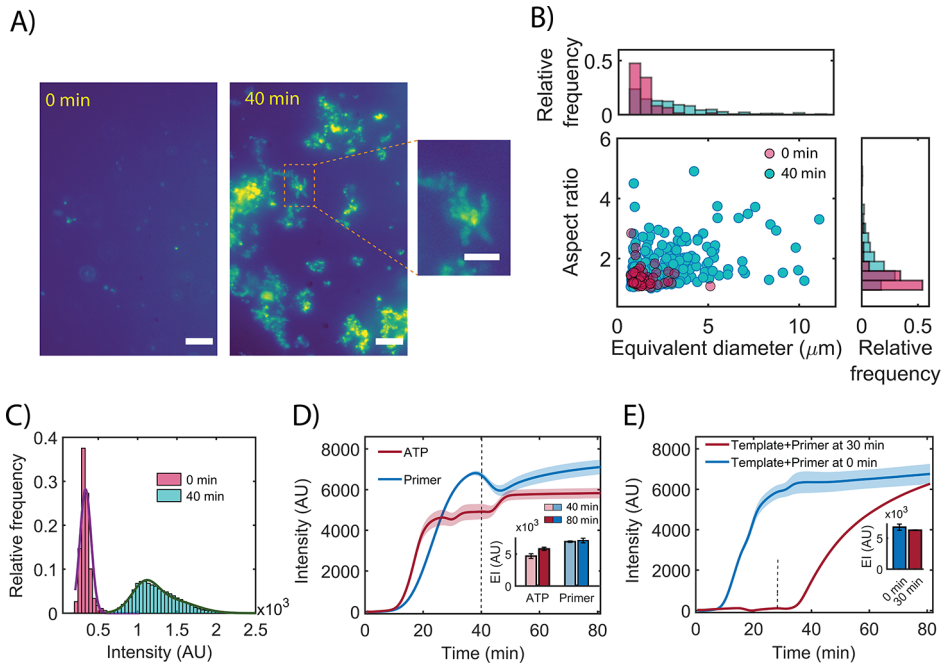

Figure 1. RPA cluster formation. (A) Fluorescent images of the RPA mix with EvaGreen DNA dye before (0 min) and after 40 min of amplification. The zoomed image highlights the branched and filamentous architecture of the nucleoprotein complexes formed. The scale bar is 10 and 5 μm for the main and zoomed images, respectively. (B) Scatter plot and marginal histograms of the aspect ratio and equivalent diameter of RPA clusters. (C) Pixel intensity histogram of RPA clusters before and after amplification. The solid smooth line represents the Gaussian fit to the intensity histograms. (D) Real-time trajectories of RPA (10^5 DNA copies) with the addition of fresh ATP or primers at 40 min (marked as dashed line) after amplification. The inset bar plot represents the average fluorescence intensity at 40 and 80 min from the time traces. (E) Real-time amplification profile with primer and template (10^5 DNA copies) added at two different time points. The blue curve indicates the addition at the start of the reaction (0 min), and the red curve indicates the addition at 30 min (dashed line) to the 39 °C preincubated mixture of RPA enzymes. The inset bar plot represents the fluorescence intensity at the end of the reaction (80 min) for both cases.

NEB: B9000S) to prevent nonspecific binding of proteins and DNA to the surface. The sample was excited with a 488 nm laser, and the emitted fluorescence was captured from different axial planes on a sCMOS camera (ORCA FLASH 4.0) with a 100× (Olympus, NA: 1.45) objective. The excitation and emission paths included a longpass dichroic filter (511 nm) and a bandpass filter (538/40 nm) (Semrock), respectively.

The captured fluorescent images of the RPA mix are analyzed using a custom-written MATLAB script. Initially, the algorithm finds the maximum intensity projection from 20 z-stack images (at 1 μm steps). The background intensities are calculated using a dilated image and subtracted from the original image. The intensity threshold is calculated from the fitting of pixel intensity histogram to a two-component Gaussian mixture model. A binarized image is generated with the thresholding applied based on this cutoff, and the connected components are merged to identify the discrete bright features (DNA clusters) in the image. The equivalent diameter (= 4 × area/perimeter) and aspect ratio (= major axis length/minor axis length) are estimated for the detected DNA clusters from the binary images.

■ RESULTS AND DISCUSSION

Nucleoprotein Cluster Formation during RPA. RPA proceeds at 39 ± 2 °C in the presence of high concentrations of co-solutes that include various DNA-binding proteins and PEG polymer. The commercial RPA cocktail is optimized for rapid DNA amplification from low target DNA levels. However, under the high concentrations of proteins, PEG, and DNA amplicons, the reaction conditions can lead to condensation and spontaneous formation of nucleoprotein clusters.[28,29]

We speculated that such aggregation would be driven by the local accumulation of new amplicons fueled by rapid DNA amplification during RPA. Indeed, the formation of RPA clusters that correlate with the starting DNA concentration has been reported recently.[30]

To examine the formation of RPA clusters, we visualize the DNA products using an intercalating dye (EvaGreen) during RPA under high magnification (100× magnification). Upon amplification, we observe the emergence of irregular aggregates with a broad size distribution and spanning up to 10 μm in effective diameter (Figure 1A,B). This is in contrast to the limited number of uniform and small puncta observed for target plasmid DNA before amplification. There is a four- to fivefold higher pixel intensity in the clusters compared to plasmid DNA, suggesting higher density of DNA in the aggregates (Figure 1C). Since recombinase and single-stranded protein (SSB) involved in RPA are known to interact and form filaments on DNA,[31] we attribute these DNA-rich aggregates to nucleoprotein clusters formed in conjunction with the recombinase and SSB complexes bound to the DNA.

We speculated that the formation of these nucleoprotein clusters could lead to a gradual inhibition of further DNA amplification. Indeed, when we supplement the reaction with additional ATP or primers after the formation of the clusters, there is negligible further amplification (Figure 1D). Alternately, to test whether the RPA reaction stalls due to the loss of protein activity over time, we added primers and template to the RPA reaction after preincubating the RPA

https://doi.org/10.1021/acs.analchem.2c02810
Anal. Chem. 2022, 94, 13897−13905

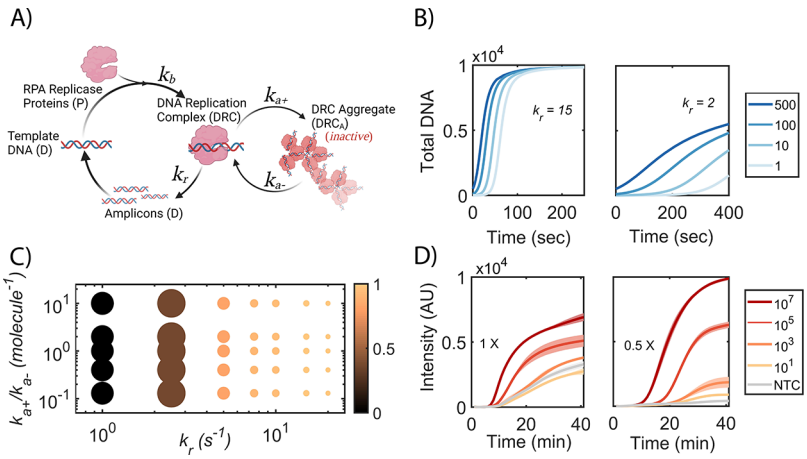

Figure 2. Model for recombinase polymerase amplification. (A) Schematic of the RPA model. (B) Model predictions for the total DNA (D_{all}) dynamics for different target DNA concentrations (left panel for k_r = 15 s^{-1} and right panel for k_r = 2 s^{-1}). The simulation parameters set are k_b = 100 molecule^{-1} s^{-1}, k_{a+} = 0.001 molecule^{-1} s^{-1}, and k_{a-} = 0.001 s^{-1}. (C) Variation in the amplicon yield and separation between amplified DNA as a function of amplification kinetic rate constants (k_r) and aggregation equilibrium (k_{a+}/k_{a-}) is shown. The color bar depicts the relative magnitude of the amplicon yield for one copy of target DNA, and the size of the circle denotes the slope of the amplicon yield between 100 and 1 DNA. (D) Real-time RPA trajectories for different RPA reaction cocktails. Left panel with the manufacturer's recommended concentration (1×) and right panel with twofold dilution. The shaded region represents the standard error (SE) from triplicates.

reaction mix (at 39 °C for 30 min). However, in this case, we observe no reduction in the final amplicon yield, suggesting that the loss of enzymatic activity is not limiting further amplification (Figure 1E). This suggests that the saturation in the RPA reaction is tied to the observed nucleoprotein cluster formation.

Model for Recombinase Polymerase Amplification. Taking cue from the experimental evidence that suggests limited amplification beyond the formation of clusters, we conjectured that varying the balance between amplification and nucleoprotein cluster formation kinetics can modulate the amplicon yields. To generate a mechanistic insight into the possible outcomes of the RPA reaction, we developed a simple kinetic model describing the production of DNA amplicons. We consolidated the RPA reaction into three distinct and broad steps, as discussed in the Materials and Methods section (Figure 2A). Our RPA reaction scheme is captured by the set of four equations (eqs 1)−4. We lumped the kinetics of DNA, protein, and primer binding in a single rapid molecular binding step with the rate constant, k_b. Similarly, extension and final product release is represented with a growth rate constant, k_r. We also include a byproduct DRC$_A$ formed from amplicons (rate constant, k_{a+}), as observed experimentally for RPA products (Figure 1A). Here, we consider polymerization to be larger than aggregation since clusters were observed only in the latter half of the RPA reaction. We also conjecture that the DRC$_A$ complex is inactive but can revert to the active form, DRC, albeit at a slow rate represented by a rate constant, k_{a-}.

Our RPA kinetic scheme displays a sigmoidal growth dynamics (as observed for the amplicon generation in RPA experiments) when the rate of amplification (k_r) is comparable or larger than the aggregation rate (k_{a+}). Additionally, the time to cross a threshold signal level (τd) increased logarithmically with the initial DNA levels. This is consistent with previous reports, and τd has been used as a parameter for the quantitative estimation of DNA with RPA.[14,32] However, with large k_r values (≥10 s^{-1}), we observe identical final amplicon levels irrespective of the initial DNA concentrations. From our model, we recognized that reduction in the polymerization rate compared to the RPA cluster formation can introduce reaction limitations that will manifest in the early termination of amplification in RPA. As k_r is reduced, we observe slower kinetics as well as reduced amplicon yield due to the premature inactivation of RPA by aggregation (Figure 2B,C). Once the available proteins drop or DRC$_A$ reaches a threshold (DRC$_{At}$), RPA stalls and reaches a plateau phase. However, this resulted in an improved separation between the threshold time and amplicon levels for different amounts of the initial DNA. Evaluating this relationship over a large range for k_r and aggregation equilibrium (k_{a+}/k_{a-}) shows that at the intermediate values of k_r, one can achieve enhanced separation between the amplicon levels without compromising the final yield significantly (Figure 2C). Therefore, apart from the threshold time of amplification, the final amplicon yield can be employed for the quantitative estimation of nucleic acids in certain RPA reaction conditions.

Modulating Amplicon Yield in RPA. To alter the kinetics of the amplification reaction, we conducted RPA under different dilutions of the reaction cocktail. Further, to reduce costs and avoid slower kinetics associated with RPA probes, we used the DNA-intercalating dye (EvaGreen) to monitor the RPA kinetics in real time. We designed RPA primers against the dengue virus capsid gene and amplified DNA segments from a plasmid with part of dengue serotype 2 virus genome. When we perform amplification with reduced amounts of RPA enzymes, the kinetics and yield of the RPA are attenuated progressively with reduction until there is poor (or no) yield (Figure S2). However, under partially reduced kinetics (at twofold dilution of the RPA mix (0.5×)), the yield of the amplified DNA was monotonically dependent on the initial target DNA concentration, as predicted by our model (Figure 2D). This is in contrast to the poor dependence of the amplicon yield on the initial DNA with the manufacturer's recommended RPA reaction conditions (termed 1×). Comparison with our model suggests that the commercial RPA kit is optimized to operate in high k_r regime to achieve rapid amplification. Another advantage of reducing amplification kinetics is the dramatic reduction in the formation of

https://doi.org/10.1021/acs.analchem.2c02810
Anal. Chem. 2022, 94, 13897−13905

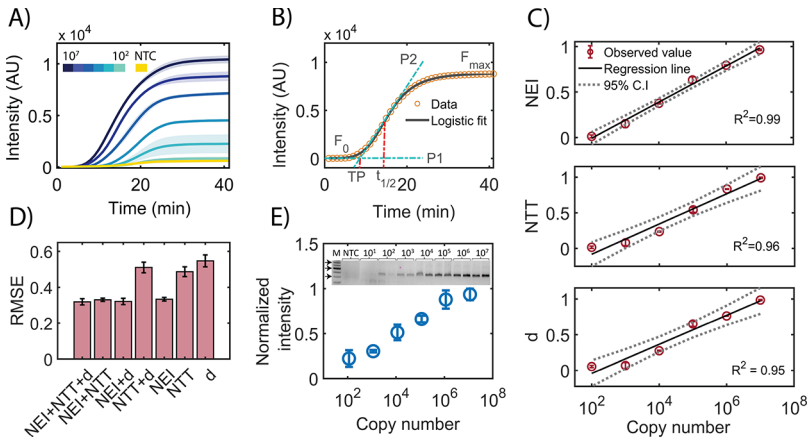

Figure 3. Estimating the target nucleic acid concentration using qeRPA. (A) The real-time RPA trajectories for serially diluted target DNA ranging from 10^7 to 10^2 molecules are plotted. The shaded region represents the SE from duplicate experiments. (B) The RPA real-time trajectory is fit to a four-parameter logistic function (eq 5). (C) The linear regression analysis of NEI and kinetic parameters is shown. The error bar represents the SE from duplicate experiments, and 95% CI is depicted between the dashed curves. (D) The RMSE from the model fit with mixed (linear and multiple linear) regression models for estimating the relationship to target DNA copy number for different factors is shown. (E) The normalized fluorescence band intensity of RPA amplicons analyzed from the gel electrophoresis is shown for different target DNA inputs. The inset represents the gel electrophoresis image corresponding to the plot. The arrow from top to bottom indicates the gel band size of 700, 500, and 300 base pairs, respectively.

nonspecific and primer-dimer products (Figure 2D and Figure S3A), enabling a simpler interpretation of RPA kinetics and amplicon yield data even with a DNA dye. We also observe heterogeneous amplification with large variation in both the threshold time and the endpoint yield even for RPA reactions at twofold dilution, which is usually a challenge for quantitative RPA (Figure S3C). However, the variability was significantly reduced when the reaction mixture was mixed thoroughly by pipetting (Figure S3C). Separately, we also verified that the specificity for the template is not compromised in the presence of mammalian genomic DNA under the enforced slower kinetics of amplification (Figure S3B).

We also note that the RPA reactions terminate in the experiments beyond 40 min. This is unlike our model predictions. Even with a reduced kinetic rate of amplification, the final amplicon yields would achieve similar levels for all input DNA upon extended incubation. We speculate that this discrepancy with our model could arise from near-complete hydrolysis of ATP or poor recovery of polymerization-competent complexes from the DRC_A state or still unknown phenomena. In spite of this, the data from Figure 1 suggests that the cluster formation is stalling further DNA amplification. We also note a moderate increase in the amplicon yields (in comparison to the recommended enzyme concentration) in some cases (e.g., compare the amplicon levels for 10^7 and 10^5 copies of DNA between 1× and 0.5× conditions in Figure 2D). This is observed despite reduced kinetics, as is evident from larger threshold times. We attribute this to the possible reduction in the rate of the RPA cluster formation affected by the dilution of the PEG and other co-solutes. Nevertheless, this demonstrates that the amplicon yield can be a monotonic function of the initial DNA level in certain RPA reaction compositions.

Establishing Nucleic Acid Quantification Using Amplicon Yield in RPA. We envisioned that the correlative end product formation can be utilized to develop a quantitative RPA without the need for real-time monitoring. For this, we evaluated the real-time RPA amplification trajectories from the serial dilution of dengue plasmid (Figure 3A). Using saturation fluorescence intensity (F_{max} at 40 min), baseline intensity (F_0), time to reach half of the fluorescence dynamic range ($t_{1/2}$), and slope of the amplification phase (d) recovered from a logistic fit, we evaluate the parameters that can report on the initial DNA concentration (Figure 3B).

We estimate the NEI that reports on the RPA amplicon yield and the NTT and slope of the amplification phase (d) that report on the kinetics and efficiency of the amplification. As is evident from the real-time RPA amplification trajectories, the NTT is linearly correlated with the log of the starting copy numbers consistent with similar reports with threshold time[14] (Figure 3C).

Additionally, a positive linear correlation is observed for the endpoint amplicon yield (reported as NEI) for a wide range of initial DNA starting from 100 to 10^7 molecules (Figure 3C). The rate of the amplification phase (d) also displays a correlated increase with the initial DNA concentration. We derive the empirical linear relationships between input DNA and all these factors individually or in combination (Figure 3C). We find that a linear regression model either with a combination of parameters with NEI or NEI alone has the least root-mean-square error (RMSE) (Figure 3D).

We further validated that NEI was an accurate estimate of target amplicon yields using gel electrophoresis (Figure 3E). Indeed, the amplicon band intensity also replicates the observed linear relationship to as low as 100 copies. Nonspecific amplification starts to interfere with target amplification below 100 copies, which sets the limit on our ability to quantify accurately below this range. Nevertheless, this shows that the amplicon yield is a robust parameter to estimate the target nucleic acid concentration over a large dynamic range and it can alleviate the need for continuous monitoring. We name this approach quantitative endpoint RPA (qeRPA). We observe the same increasing trend visually for the amplicon yield (EvaGreen fluorescence intensity) in the reaction vial post amplification (Figure S4). Therefore, qeRPA is also amenable to visual qualitative inspection of amplicons despite the overall reduction in yield and slower kinetics.

https://doi.org/10.1021/acs.analchem.2c02810
Anal. Chem. 2022, 94, 13897−13905

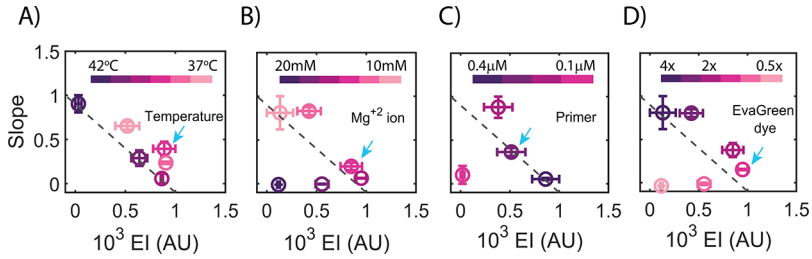

Figure 4. Efficiency of the qeRPA reaction under different conditions. The *x*-axis and *y*-axis represent the normalized endpoint intensity of 1000 DNA copies and slope of NEI vs log(copy number) for each dataset. qeRPA performance as a function of (A) temperature: 42 to 37 °C with an interval of 1 °C; (B) Mg^{+2} ion: 20, 18, 16, 14, 12, and 10 mM; (C) primer concentration from 0.4 to 0.1 μM with a 0.1 μM interval; (D) EvaGreen dye: 4×, 3×, 2×, 1.5×, 1×, and 0.5×, where 1× corresponds to 1.36 μM. The blue arrow in each plot denotes the condition employed in the optimized qeRPA. The dashed gray line is a visual aid to demarcate qeRPA performance with conditions on or above the line considered acceptable. The error bar represents the SE from duplicate experiments.

We also verify that the RPA kinetics and the endpoint amplicon yield for qeRPA can be captured with specific DNA-based RPA probes. Consistent with DNA dye-based qeRPA, we observe that the final amplicon yield is a function of the initial target DNA level (Figure S5). However, a slower kinetics was observed for probe-based qeRPA, suggesting that probe binding and processing is the rate limiting step. On the other hand, the increased specificity of probes results in a better signal-to-noise ratio for the amplicon yield (inset in Figure S5). Therefore, endpoint amplicon-based qeRPA can be applied irrespective of the choice of detection strategy for the amplicon yield. Combined with challenges in designing efficient RPA probes and associated costs, we argue that DNA dye-based detection is a better reporter for RPA dynamics, and hence, we chose EvaGreen for further characterizing qeRPA.

Robustness of qeRPA under Various Reaction Conditions. Since the modifications to the RPA reaction enabling qeRPA can compromise the reaction under diverse conditions, we examined whether and when qeRPA fails. To determine the robustness of qeRPA, we examined the effect of various factors (temperature, primer, and magnesium levels) on amplification and subsequent quantification. For a quick evaluation of qeRPA under various conditions, we compare dengue amplicon yields (reported for 1000 DNA copies) and the extent of separation in the amplicon yield between low and high DNA concentration regimes (estimated as the slope between the amplicon yields at 1000 and 1 million copies of target DNA). These two criteria define the detectable signal (sensitivity) and the resolution for DNA estimation by qeRPA and are depicted on two orthogonal axes for each condition (Figure 4). The recommended operating temperature ranges from 37 to 42 °C for RPA. At temperatures above 40 °C, either the amplicon yield or separation between copy numbers is compromised, but at all other conditions, qeRPA should perform comparable to each other (Figure 4A). Additionally, at all the temperatures below 42 °C, qeRPA generated specific products and fewer nonspecific products, as observed by gel electrophoresis (data not shown).

Magnesium serves as a cofactor for UvsX recombinase and Sau DNA polymerase in RPA and affects the stability of the duplex DNA. Between 12 and 16 mM, RPA generates specific amplicons, with detectable amplicon yields, and optimal separation for quantification with qeRPA. However, at 10 mM Mg^{+2}, the RPA amplicon yield is poor, and at concentrations above 16 mM, there is poor resolution in distinguishing DNA levels (Figure 4B). Therefore, the optimal window of magnesium concentration is consistent with the recommended conditions for conventional RPA.[33] The optimum concentration of primer is critical for specific product formation against the backdrop of template-free primer extension products. Moreover, recombinase-bound primer levels are expected to define the amplification rate in RPA, and hence, recombinase-primer stoichiometry is a key parameter. Figure 4C suggests a 0.2 μM primer concentration as the best-performing condition with a large value for the slope and endpoint intensity. However, with an increase in the primer concentration (from 0.2 to 0.4 μM), the endpoint intensity increases but results in a reduced separation between the amplicon levels. This is expected from an increase in the amplification rate (k_r) consistent with our model (Figure 1B). At lower primer concentrations (0.1 μM), the amplicon yield is less predictive for quantification due to the poor amplification.

We also examined the effect of the DNA dye on qeRPA resolution and yield. EvaGreen dye at 2.04−4.08 μM (corresponding to 1.5×−3× fold of that recommended for qPCR) for real-time detection in qeRPA displayed high signal intensity and resolution. Lower dye concentrations (≤1×) do not provide sufficient distinction between the different DNA levels due to the poor dye : DNA stoichiometry. On the other hand, higher dye concentration (4×) resulted in reduced amplicon yield, indicating the inhibitory effects of EvaGreen dye on RPA (Figure 4D).

Due to the limitations placed on the amplification kinetics, we identify an overall inverse relationship between the amplicon yield and the resolution of qeRPA (Figure 4). Nevertheless, we argue that qeRPA performance is generally robust over conditions consistent with RPA protocols. Based on this analysis, we recommend incubation at 39 °C for 40 min with twofold dilution of RPA master mix, 14 mM magnesium, 0.3 μM primers, and 2.04 μM EvaGreen dye for qeRPA.

Quantification of Dengue Viral RNA from Patient Serum. To demonstrate the clinical applicability of qeRPA, we next determined the viral RNA in the patient serum samples with active dengue virus infection (Figure 5B). With a new set of primers designed against the conserved regions in the capsid gene of the dengue serotype 2 genomes prevalent in India, we confirmed specificity and sensitivity for qeRPA (Figure S6).[34] We re-evaluated qeRPA with these primer sets and determined optimal conditions to be 0.3 μM primers, 14 mM Mg^{+2}, and 40 °C, which was consistent with previously characterized conditions for qeRPA.

Viral cDNA generated from purified serum RNA are quantified by qPCR and compared to qeRPA estimates. The

https://doi.org/10.1021/acs.analchem.2c02810
Anal. Chem. 2022, 94, 13897−13905

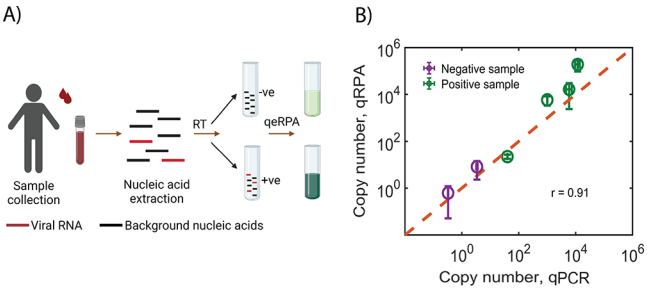

Figure 5. Viral RNA quantification from clinical samples. (A) The blood serum from dengue virus-infected patients is collected, and RNA extracted is reverse transcribed (RT) to cDNA. The samples with dengue viral cDNA show an increased fluorescence signal compared to the negative samples devoid of viral cDNA. (B) The comparison of the copy numbers calculated by two methods (qPCR and qeRPA) is shown. The dashed line indicates the concordance line for qPCR and qeRPA. The error bar represents the SE from triplicate experiments.

Ct values for qPCR with the RPA primers for two control samples (C1 and C2) were >31 and for all the four positive samples (P1−P4) tested were <29. We estimated the viral cDNA copy numbers from qPCR using the standard curve generated with the pRL02 plasmid (Figure S6A). Similarly, for qeRPA, the standard curve is generated using NEI after amplification (Figure S6B). Viral nucleic acid levels quantified with qeRPA are concordant with the qPCR estimates for all the positive samples (Figure 5B). The qeRPA was able to predict the copy numbers reliably (r = 0.91), and the largest variation observed at the highest viral load was within a log order of magnitude from the qPCR estimate. Interestingly, we could detect specific amplification of the dengue amplicon with qeRPA even below 100 copies (sample P4; Figure S6C). Even for control samples (with no specific target band), the level of nonspecific amplification was comparable between qPCR and qeRPA. This suggests that further RPA primer optimization can improve the detection limit in qeRPA. Nevertheless, the qeRPA method can accurately estimate the concentration of viral nucleic acids from clinical samples.

■ CONCLUSIONS

Insights from fluorescence imaging of RPA end products led to the realization that the formation of nucleoprotein clusters is a crucial feature in the RPA reaction. Using a mathematical model that incorporates nucleoprotein cluster formation for the first time, we identify and leverage the competing reactions, namely, DNA amplification and nucleoprotein cluster formation in RPA by altering their kinetics. We show that this results in the endpoint amplicon amounts correlating with the starting DNA amounts. Here, we present this optimized semiquantitative isothermal method, qeRPA, that bypasses the requirement for continuous monitoring. The method was able to accurately detect and quantify target nucleic acids over a large dynamic range in less than an hour and was robust over most reaction conditions. In contrast to other methods that rely on the time of amplification onset as a parameter, qeRPA is less susceptible to errors as the tight control of the onset of the reaction is no longer critical. Further improvisation in the primer design or the RPA reaction mix composition can reduce nonspecific products and further increase amplicon yields and their separation in qeRPA. Alternatively, the usage of target-specific probes will also enhance the specificity and sensitivity of the qeRPA method. Overall, a sensitive amplification strategy that accurately recapitulates the initial stoichiometry of DNA species after amplification can find usage in other areas like metagenomics and single-cell sequencing.

■ ASSOCIATED CONTENT

Supporting Information

The Supporting Information is available free of charge at https://pubs.acs.org/doi/10.1021/acs.analchem.2c02810.

Additional figures presenting the RPA dynamics, sequence of primers and probe, modeling parameters, accession numbers of Indian dengue 2 virus genomes included in the study, and detailed derivation for RPA threshold time (PDF)

■ AUTHOR INFORMATION

Corresponding Author

Rahul Roy − *Department of Chemical Engineering and Center for BioSystems Science and Engineering, Indian Institute of Science, Bangalore, Karnataka, India 560012;* orcid.org/0000-0003-3329-8803; Email: rahulroy@iisc.ac.in

Author

Priyanka Valloly − *Department of Chemical Engineering, Indian Institute of Science, Bangalore, Karnataka, India 560012*

Complete contact information is available at: https://pubs.acs.org/10.1021/acs.analchem.2c02810

Notes

The authors declare no competing financial interest.

■ ACKNOWLEDGMENTS

The authors thank Twinkle Gupta and Suraj Jagtap for their help with the primer design for Indian dengue genomes and Saranya Marimuthu for sharing the plasmid pRL02. This work was supported by the Department of Science and Technology, DST-SERB grant CRG/2018/004266 (R.R.), Department of Biotechnology, DBT Biodesign-Bioengineering Initiative BT/PR13926/MED31/97/2010 (R.R.), and PhD fellowship from the Indian Institute of Science (P.V.).

■ REFERENCES

(1) VanGuilder, H. D.; Vrana, K. E.; Freeman, W. M. *BioTechniques* **2008**, *44*, 619−626.
(2) Gullett, J. C.; Nolte, F. S. *Clin. Chem.* **2015**, *61*, 72−78.
(3) Gonzalez-Pena, V.; Natarajan, S.; Xia, Y.; Klein, D.; Carter, R.; Pang, Y.; Shaner, B.; Annu, K.; Putnam, D.; Chen, W.; et al. *Proceedings of the National Academy of Sciences* **2021**, *118*, e2024176118.
(4) Mullis, K.; Faloona, F.; Scharf, S.; Saiki, R.; Horn, G.; Erlich, H. *Cold Spring Harbor Symp. Quant. Biol.* **1986**, *51*, 263−273.
(5) Higuchi, R.; Dollinger, G.; Walsh, P. S.; Griffith, R. *Bio/Technology* **1992**, *10*, 413−417.
(6) Zhao, Y.; Chen, F.; Li, Q.; Wang, L.; Fan, C. *Chem. Rev.* **2015**, *115*, 12491−12545.
(7) Notomi, T.; Okayama, H.; Masubuchi, H.; Yonekawa, T.; Watanabe, K.; Amino, N.; Hase, T. *Nucleic Acids Res.* **2000**, *28*, e63.
(8) Ma, F.; Liu, M.; Tang, B.; Zhang, C.-y. *Anal. Chem.* **2017**, *89*, 6182−6187.
(9) Nadeau, J. G.; Pitner, J. B.; Linn, C. P.; Schram, J. L.; Dean, C. H.; Nycz, C. M. *Anal. Biochem.* **1999**, *276*, 177−187.

(10) Nixon, G. J.; Svenstrup, H. F.; Donald, C. E.; Carder, C.; Stephenson, J. M.; Morris-Jones, S.; Huggett, J. F.; Foy, C. A. *Biomol. Detect. Quantif.* **2014**, *2*, 4−10.
(11) He, D.; Yang, J.; Jiang, X.; Lin, Y.; Chen, H.; Tang, Y.; Diao, Y. *Poult. Sci.* **2020**, *99*, 6586−6592.
(12) Piepenburg, O.; Williams, C. H.; Stemple, D. L.; Armes, N. A. *PLoS Biol.* **2006**, *4*, No. e204.
(13) Li, J.; Macdonald, J.; von Stetten, F. *Analyst* **2018**, *144*, 31−67.
(14) Crannell, Z. A.; Rohrman, B.; Richards-Kortum, R. *Anal. Chem.* **2014**, *86*, 5615−5619.
(15) Khan, M. A. A.; Faisal, K.; Chowdhury, R.; Ghosh, P.; Hossain, F.; Weidmann, M.; Mondal, D.; Abd El Wahed, A. *Diagnostics* **2021**, *11*, 1963.
(16) Cantera, J. L.; White, H. N.; Forrest, M. S.; Stringer, O. W.; Belizario, V. Y., Jr.; Storey, H. L.; de Hostos, E. L.; de Los Santos, T. *PLoS Neglected Trop. Dis.* **2021**, *15*, No. e0009782.
(17) Lillis, L.; Lehman, D.; Singhal, M. C.; Cantera, J.; Singleton, J.; Labarre, P.; Toyama, A.; Piepenburg, O.; Parker, M.; Wood, R.; et al. *PLoS One* **2014**, *9*, No. e108189.
(18) Mancuso, C. P.; Lu, Z.-X.; Qian, J.; Boswell, S. A.; Springer, M. *Anal. Chem.* **2021**, *23*, 9541.
(19) Toley, B. J.; Covelli, I.; Belousov, Y.; Ramachandran, S.; Kline, E.; Scarr, N.; Vermeulen, N.; Mahoney, W.; Lutz, B. R.; Yager, P. *Analyst* **2015**, *140*, 7540−7549.
(20) Moody, C.; Newell, H.; Viljoen, H. *Biochem. Eng. J.* **2016**, *112*, 193−201.
(21) Weusten, J. J.; Carpay, W. M.; Oosterlaken, T. A.; van Zuijlen, M. C.; van de Wiel, P. A. *Nucleic Acids Res.* **2002**, *30*, e26−e26.
(22) Gordon, M. I.; Klemer, D. P.; Fuller, S. L.; Chang, J. H.; Klemer, D. R.; Putnam, M. L. *Eng. Rep.* **2019**, *1*, No. e12047.
(23) Galletto, R.; Amitani, I.; Baskin, R. J.; Kowalczykowski, S. C. *Nature* **2006**, *443*, 875−878.
(24) Ringrose, L.; Lounnas, V.; Ehrlich, L.; Buchholz, F.; Wade, R.; Stewart, A. F. *J. Mol. Biol.* **1998**, *284*, 363−384.
(25) Langer, A.; Schräml, M.; Strasser, R.; Daub, H.; Myers, T.; Heindl, D.; Rant, U. *Sci. Rep.* **2015**, *5*, 1−15.
(26) Subramanian, S.; Gomez, R. D. *PLoS One* **2014**, *9*, No. e100596.
(27) Hua, B.; Han, K. Y.; Zhou, R.; Kim, H.; Shi, X.; Abeysirigunawardena, S. C.; Jain, A.; Singh, D.; Aggarwal, V.; Woodson, S. A.; Ha, T. *Nat. Methods* **2014**, *11*, 1233−1236.
(28) Claeys Bouuaert, C.; Pu, S.; Wang, J.; Oger, C.; Daccache, D.; Xie, W.; Patel, D. J.; Keeney, S. *Nature* **2021**, *592*, 144−149.
(29) Powell, M. L.; Bowler, F. R.; Martinez, A. J.; Greenwood, C. J.; Armes, N.; Piepenburg, O. *Anal. Biochem.* **2018**, *543*, 108−115.
(30) Sullivan, B. P.; Chou, Y.-S.; Bender, A. T.; Martin, C. D.; Kaputa, Z. G.; March, H.; Song, M.; Posner, J. D. Quantitative Isothermal Amplification on Paper Membranes using Amplification Nucleation Site Analysis. *Lab on a Chip* **2022**.
(31) Wu, H.-Y.; Lu, C.-H.; Li, H.-W. *Sci. Rep.* **2017**, *7*, 1−13.
(32) Bender, A. T.; Borysiak, M. D.; Levenson, A. M.; Lillis, L.; Boyle, D. S.; Posner, J. D. *Anal. Chem.* **2018**, *90*, 7221−7229.
(33) Li, J.; Ma, B.; Fang, J.; Zhi, A.; Chen, E.; Xu, Y.; Yu, X.; Sun, C.; Zhang, M. *Foods* **2020**, *9*, 27.
(34) Kar, M.; Nisheetha, A.; Kumar, A.; Jagtap, S.; Shinde, J.; Singla, M.; Saranya, M.; Pandit, A.; Chandele, A.; Kabra, S. K.; et al. *Int. J. Infect. Dis.* **2019**, *84*, S25−S33.

Recommended by ACS

Multiplex Assay of Viruses Integrating Recombinase Polymerase Amplification, Barcode—Anti-Barcode Pairs, Blocking Anti-Primers, and Lateral Flow Assay

Alexandr V. Ivanov, Boris B. Dzantiev, *et al.*
SEPTEMBER 29, 2021
ANALYTICAL CHEMISTRY
READ

Microfluidic Biosensor for Rapid Nucleic Acid Quantitation Based on Hyperspectral Interferometric Amplicon-Complex Analysis

Rongxin Fu, Guoliang Huang, *et al.*
OCTOBER 25, 2021
ACS SENSORS
READ

Determination of Advantages and Limitations of qPCR Duplexing in a Single Fluorescent Channel

Haoqing Zhang, Pavel Neuzil, *et al.*
AUGUST 19, 2021
ACS OMEGA
READ

Multiplex Visualized Closed-Tube PCR with Hamming Distance 2 Code for 15 HPV Subtype Typing

Jixue Weng, Qinxin Song, *et al.*
MARCH 22, 2021
ANALYTICAL CHEMISTRY
READ

Get More Suggestions >

https://doi.org/10.1021/acs.analchem.2c02810
Anal. Chem. 2022, 94, 13897−13905